Variable-density k-space filling curves for accelerated Magnetic Resonance Imaging

Carole Lazarus, Pierre Weiss, N. Chauffert, F. Mauconduit, Loubna El Gueddari, Christophe Destrieux, I. Zemmoura, A. Vignaud, Philippe Ciuciu

Variable-density k-space filling curves for accelerated Magnetic Resonance Imaging

C. Lazarus[1,2,3], P. Weiss[4,5,6], N. Chauffert[1], F. Mauconduit[7], L. El Gueddari[1,2,3], C. Destrieux[8], I. Zemmoura[8], A. Vignaud[1,2] & P. Ciuciu[1,2,3]

[1]*NeuroSpin, CEA Saclay, 91191 Gif-sur-Yvette cedex, France*
[2]*Université Paris-Saclay, France*
[3]*Parietal, INRIA, 91120 Palaiseau, France*
[4]*ITAV USR3505 CNRS, 31000 Toulouse, France*
[5]*IMT UMR 5219 CNRS, 31400 Toulouse, France*
[6]*Université de Toulouse, France*
[7]*Siemens Healthineers, 93210 Saint-Denis, France*
[8]*Université François-Rabelais de Tours, INSERM, Imagerie et Cerveau UMR 930, 37000 Tours, France*

Reducing scan times in magnetic resonance imaging (MRI) is essential for attaining high spatial resolution, which could aid in diagnosing certain pathologies, such as Alzheimer's disease. Methods to accelerate the time of segmented MR acquisitions commonly rely on simple sampling patterns such as straight lines, spirals or slight variations of these elementary shapes. However, such geometrical approaches do not take full advantage of the degrees of freedom offered by the hardware and cannot be easily adapted to fit an arbitrary sampling distribution. Here, we report the use of a versatile method inspired from stippling techniques that automatically generates optimized sampling patterns compatible with MR hardware constraints on maximum gradient amplitude and slew rate. These non-Cartesian sampling curves are designed to comply with key criteria for optimal sampling: a controlled distribution of samples and a locally uniform k-space coverage. Combining sampling efficiency with compressed sensing, the resulting sampling patterns allowed up to 20-fold reductions in MR scan time (compared to fully-sampled Cartesian acquisitions) for two-dimensional T_2^*-weighted imaging without deterioration of image quality, as demonstrated by our experimental results at 7 Tesla on *in vivo* human brains for a high in-plane resolution of 390 μm. In comparison to existing non-Cartesian sampling strategies (spiral and radial), the proposed technique also yielded superior image quality. Since our method does not involve additional hardware, this approach offers a cost-free solution that has the potential to improve sampling efficiency in many MRI applications.

Magnetic resonance imaging (MRI) is one of the most powerful and safest imaging modalities for examining the human body. High-resolution MRI is expected to aid in the understanding and diagnosis of many neurodegenerative pathologies involving submillimetric lesions or morphological changes, such as Alzheimer's disease and multiple sclerosis[1–3]. Although high-magnetic-field systems can deliver a sufficient signal-to-noise ratio (SNR) to increase spatial resolution[4], long scan times and motion sensitivity continue hindering the utilization of high resolution MRI.

Despite the development of corrections for bulk and physiological motion[5–8], long acquisition times remain a major obstacle to high-resolution acquisition, especially in clinical applications.

In MRI, an image is acquired indirectly through its Fourier transform, which represents its spatial frequency content. More precisely, the Fourier domain, referred to as the *k-space*, is sampled along parameterized curves generated by varying magnetic field gradients. Owing to hardware and physiological constraints (e.g., peripheral nerve stimulations), these encoding gradients have a bounded amplitude and a maximum slew rate, imposing limitations of speed and acceleration on the sampling trajectories. In addition, the rapid decay of the MR signal prevents the measurement of all the needed data at once. For these reasons, MR sampling is generally performed sequentially using segmented sampling patterns composed of multiple shots. Filling the entire k-space array may thus require a long imaging time especially for high-resolution imaging. In this work, we make significant progress in accelerating the time of segmented MR acquisitions with minimum deterioration of image quality, by limiting the number of shots using optimized sampling patterns. The proposed strategy can be used in combination with parallel imaging[9,10], yielding even more important acceleration factors.

Most MRI sampling methods are currently based on the Shannon-Nyquist theory, which relies on the use of Cartesian sampling, with the number of required samples increasing with the resolution. The newly developed theory of compressed sensing[11–13] offers a promising solution for reducing the MRI scan time, since it theoretically allows for subsampling of the k-space while guaranteeing exact reconstructions. While early theoretical results were based on concepts such as incoherence or restricted isometry properties, more recent developments[14,15] suggest compliance with two criteria for optimal sampling:

(i) The sampling pattern should be distributed along a given variable density. In the case of MRI, low frequencies should be sampled more densely than high frequencies.

(ii) Coverage of the k-space should be locally uniform to avoid large gaps and clusters of samples.

Although seemingly unrelated, the Shannon-Nyquist and compressive sampling theories advocate for the same criteria since both methods promote *locally uniform sampling patterns* and differ only in the target density (uniform density for the Shannon-Nyquist theory and variable density for compressed sensing theory). Methods to generate sampling patterns satisfying (i) and (ii) have been extensively studied and range from simple dart throwing to Poisson disk sampling or more elaborate optimal transportation-based techniques[16,17]. Nevertheless, since they do not account for hardware constraints and produce discontinuous samples, these algorithms are unable to provide sampling curves for MRI.

This limitation may explain why the 2D sampling patterns used in practice are essentially

made of simple analytical models such as Cartesian lines[18,19], non-Cartesian radial spokes[20–22], spiral interleaves[23,24] and variations of these patterns[25–29]. Although these geometrical curves may enable relatively rapid scanning, they do not take advantage of all the degrees of freedom offered by the hardware and lack flexibility to comply with the above optimal criteria. They may therefore be significantly improved to reduce MRI scan time.

Here, we introduce a method called SPARKLING, that may overcome these limitations by taking a radically new approach to the design of k-space sampling. The acronym SPARKLING stands for Spreading Projection Algorithm for Rapid K-space sampLING. To optimally spread the samples (criteria (i)-(ii)), our method relies on optimization to automatically generate k-space trajectories under the aforementioned hardware constraints by minimizing a tailored distance between the sample distribution and any prescribed density (for details, see Materials and Methods). Finally, to maximize sampling efficiency (i.e., the k-space coverage per unit time), we apply our algorithm to highly-sampled trajectories in the same manner as for spiral imaging[30]. Hence, for a given MR protocol with defined imaging parameters (TR, TE and readout duration), this method is able to enhance sampling performance.

The proposed sampling patterns were prospectively validated both *ex vivo* and *in vivo* in healthy volunteers on a 7-Tesla MR scanner for T_2^*-weighted imaging. The versatility of the method was demonstrated for various setups and target densities. In comparison to standard fully-sampled Cartesian acquisitions, our strategy significantly reduced the scan time while maintaining good image quality. Moreover, SPARKLING-generated acquisitions were compared to acquisitions obtained with two non-Cartesian sampling methods widely used in anatomical MRI, namely, radial and spiral trajectories. Using the same equally accelerated gradient echo sequence (GRE) and without additional equipment, we show that our method achieves enhanced image quality. The stability of SPARKLING-generated acquisitions was also tested for very high in-plane acceleration factors of up to 20.

Results

The flowchart describing our method is depicted in (Fig. 1). Any segmented pattern (feasible or not) may serve as an initialization of the proposed pipeline and be transformed into a feasible k-space trajectory with a truly controlled density and optimized k-space coverage. Gradient waveforms are defined as a set of discrete gradient amplitudes that are spaced across a given gradient sampling period, defined as the *raster time*. The latter is fixed and typically equal to $dt = 10\ \mu s$ on the actual MR gradient coils. The support of a k-space trajectory is thus determined by its gradients steps and will be sampled at the desired sampling rate, also referred to as the readout bandwidth (rBW $= \frac{1}{\Delta t}$, where Δt is the interval between digitized samples also called *dwell time*).

Optimized distribution. The key aspect of our method is optimization, in which the samples are optimally distributed in the non-Cartesian k-space, following criteria (i)-(ii). More precisely, a L^2 distance between the desired density and the sample distribution is minimized under the constraints

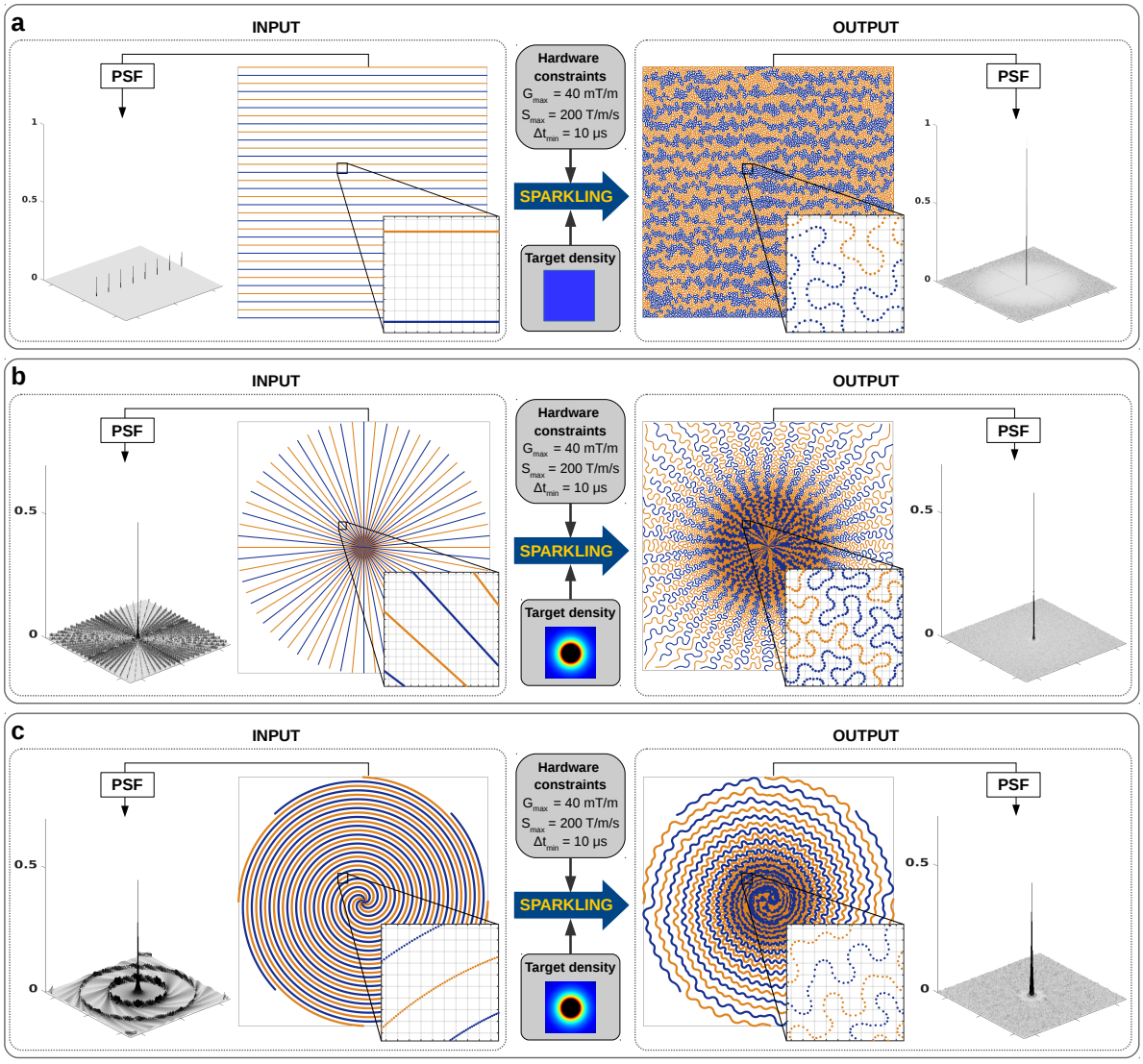

Figure 1: **Generation of SPARKLING trajectories for different initializations and target densities**. The maximum gradient amplitude and slew rate were $G_{max} = 40$ mT/m and $S_{max} = 200$ T/m/s, respectively. The duration of each segment was 30.72 ms, and the readout bandwidth was taken equal to the gradient bandwidth (rBW = $\text{BW}_{\text{gradient}} = 100$ kHz). **a**, The SPARKLING method applied to Cartesian lines with uniform density for $N = 256$ and 32 segments ($AF = 8$, $R = 0.66$). **b**, The SPARKLING method applied to radial spokes with variable radial density for $N = 512$ and 34 symmetric segments ($AF = 15$, $R = 2.5$). **c**, The SPARKLING method applied to centered-out Archimedean spiral initialization with variable radial density for $N = 256$ and 8 segments ($AF = 32$, $R = 2.66$).

of a maximum gradient (G_{max}) and a maximum slew rate (S_{max}) by means of a projected gradient descent[31]. This distance is expressed as a potential energy containing an attractive term (bringing together samples according to the target density) and a repulsive term (avoiding the formation of gaps and clusters of samples). When using compressed sensing, since the selection of the target density proved to be important for optimal results, we incorporated in our method a density generator that adapts to the resolution and the number of samples (for details, see Materials and Methods). Finally, the method allows to handle of additional linear constraints such as passage through the origin of the k-space at a given time (the *echo time*), which is crucial for controlling the image contrast. In all experiments, the maximum gradient amplitude and slewrate were set to standard hardware values on MR systems: $G_{max} = 40\,\text{mT/m}$ and $S_{max} = 200\,\text{T/m/s}$.

High sampling rate. To take full advantage of the curves' flexibility and maximize sampling efficiency, it seems natural to sample at least at the same rate as the gradient bandwidth. The same idea guides spiral acquisitions, where a high sampling rate is used to rapidly sweep over a large portion of the k-space[30,32]. Although a higher readout bandwidth practically increases the amount of noise per sample, the resulting additional information collected is theoretically more advantageous[33].

More importantly, one has to keep in mind that although k-space trajectories traverse a continuous path, the signal is sampled only at discrete intervals along the path. Because of the underlying bandlimiting filters of MR receiver hardware, the measured information is essentially averaged over pieces of trajectories comprised between two sampled points[34–36]. Hence, it is necessary to incorporate a third criterion in our trajectory design to minimize these filtering effects:

(iii) For each individual shot, assuming a certain sampling rate rBW, the k-space path between two consecutive samples should be smaller than the size of a k-space pixel $\Delta k = \frac{1}{\text{FOV}}$, where FOV is the field-of-view.

This additional requirement tends to straighten the trajectories, since they are designed so that consecutively acquired samples remain close to each other in the k-space. To relax this side effect, the readout sampling rate should therefore be chosen as large as possible. Indeed, as the sampling rate increases, more and more circumvolutions are permitted to fill the k-space, as is illustrated in (Fig. 2). Hence, using a high sampling rate allows for improvement of the resolution in the k-space, which is critical in the case of our non-Cartesian winding trajectories (see more discussion in Materials and Methods).

Altogether, in all our experiments, we acquired the ADC samples at a rate of 100 kHz, which is equal to the gradient bandwidth: ADC samples and gradient samples are thus superimposed. Because MR data are sampled at a high rate and samples are optimally spread along a variable density adapted to compressed sensing, the proposed method allows to maximize the amount of

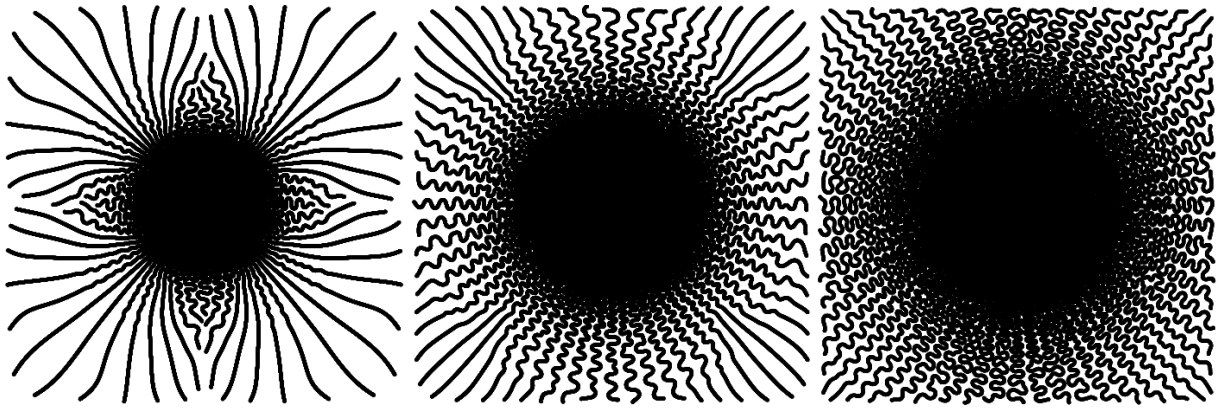

Figure 2: **Evolution of SPARKLING patterns as a function of the readout sampling rate**. Radial-initialized SPARKLING trajectories composed of 34 shots were generated for three growing readout sampling rates. From left to right, the readout bandwidth (rBW) is equal to 25 kHz, 50 kHz and 100 kHz respectively. Because the k-space path between two consecutive samples acquired along an individual shot is constrained to be smaller than the size of a k-space pixel ($\Delta k = 5$ m^{-1}), the trajectories become more flexible and space-filling as the rBW increases. Excluding the readout sampling rate, all other parameters were kept constant and the same radially decaying target density was used. The readout duration was 30.72 ms, corresponding to 3072 gradient steps (displayed on the figures) per individual shot ($\text{BW}_{\text{gradient}} = 100$ kHz). The considered imaging matrix was 512×512, corresponding to a resolution of 390 μm $\times$ 390 μm.

information measured per shot, and thus to reduce the large number of shots needed for high resolution imaging. Hence, very high acceleration factor AF can be achieved while maintaining a relatively low subsampling factor R. R and AF are defined with respect to the fully sampled Cartesian acquisition (ground truth image), leading to the formulas $R = n/m$ and $AF = N/n_c$, where $n = N \times N$ is the number of pixels in the image, m is the number of collected Fourier samples and n_c is the number of shots.

Uniform sampling. To illustrate the versatility of the proposed approach, we first consider a uniform density without undersampling for an acceleration factor of $AF = 8$ and an imaging matrix of 256×256. Classically, the fully sampled Cartesian acquisition would measure 512 samples (oversampling factor of 2) along 256 Cartesian lines to fill the k-space grid. (Fig. 1a) displays how our process transforms an initial Cartesian trajectory composed of 32 parallel lines, which corresponds to $AF = 8$. Here, the considered readout duration is 30.72 ms, corresponding to 3072 samples (rBW = $\text{BW}_{\text{gradient}} = 100$ kHz), with the idea to perform T_2^*-weigthed acquisitions[37]. Our optimization algorithm deforms these straight lines and uniformly scatters the non-Cartesian samples along highly sinuous curves. In this case, despite high acceleration ($AF = 8$), the acquisition is not subsampled ($R = 0.66$). (Supplementary video 1) shows the generation of the SPARKLING sampling in (Fig. 1a) and illustrates how samples are spread to maximize coverage.

Variable-density sampling. Above all, the most important benefit of our strategy where the largest acceleration factors are attained lies in the use of variable densities. Hence, in the context of compressed sensing, our approach can substantially improve robustness to subsampling by complying with criteria (i)-(ii). The results of such variable-density k-space trajectories are presented for a radial initialization in (Fig. 1b) and for an Archimedean spiral initialization in (Fig. 1c). In both cases, the input initializations did not originally comply with the gradient hardware constraints, the target density was radially decreasing, and the considered readout duration was also 30.72 ms. (Supplementary video 2) shows the dynamic generation of the SPARKLING sampling in (Fig. 1b). (Fig. 1a-c) also displays the point spread functions (PSFs) of both the input and output k-space trajectories, defined as the modulus of the Fourier transform of the sampling pattern viewed as a set of Dirac impulses. This result shows how the proposed method improves the PSF properties by transforming coherent patterns that are sources of artifacts into incoherent noise, which is easily removed with nonlinear reconstructions. The output central peak is also better defined than initially and is surrounded by a low-energy annulus, yielding higher image quality[38,39].

Prospective validation of SPARKLING. The proposed method was prospectively validated on a 7-Tesla MR scanner with a modified gradient echo (GRE) sequence, allowing to execute any feasible gradient waveform. All acquisitions were prospectively performed with this sequence for both *ex vivo* and *in vivo* acquisitions and a 32-channel receiver coil was used. The first set of experiments involved an *ex vivo* human brain, which allowed assessing the performance of the proposed strategy independently from motion and physiological considerations. Second, acquisitions were also performed *in vivo* on four healthy volunteers to validate the clinical potential of the approach. Following typical high-field sequence specifications[37], we considered a T_2^* contrast with an echo time of 30 ms and a readout of 30.72 ms for both *in vivo* and *ex vivo* experiments. The long repetition time (550 ms) allows to acquire 11 interleaved slices per excitation, but in what follows, reconstructions are only displayed for one slice. To assess the performance of our method, we compared it with the two most widespread non-Cartesian trajectories in MRI: radial and variable-density spiral trajectories (Materials and Methods, Fig. 9). The collected mutli-channel non-Cartesian data were reconstructed using a ℓ^1-based nonlinear reconstruction algorithm suggested in compressed sensing, which does not account for distortions[40,41].

Ex vivo experiments. Prospective results of the SPARKLING strategy initialized with Cartesian lines for a T_2^*-weighted contrast are displayed in (Fig. 3) in the case of the uniform-density output shown in (Fig. 1a). The acquisition performed with the SPARKLING trajectories thus lasted 16 s, which is 8 times shorter than the fully sampled Cartesian acquisition with an acquisition duration of 2 min 20 s for 11 slices. SPARKLING images reconstructed with nonlinear compressed sensing reconstructions are displayed in (Fig. 3b-f). We also show in (Fig. 3c-g) the results of a simple gridding method to reconstruct the SPARKLING data. Both reconstructions show very little difference from the fully sampled Cartesian reference (Fig. 3a-e), although the gridding reconstruction may be slightly noisier (Fig. 3g) than the nonlinear reconstruction (Fig. 3f). The data corresponding to the input trajectory of 32 Cartesian lines (oversampled by a factor of 2) in (Fig. 1a) can be typi-

cally processed online with a GRAPPA reconstruction[10] available on the MR scanner to produce the image in (Fig. 3d-h). The degradation of the image quality, along with a significant decrease in the SNR, is clearly observed (Fig. 3h).

The radially initialized SPARKLING strategy similar to that in (Fig. 1b) was also compared to widely used radial and variable-density spiral trajectories for an in-plane resolution of 780 μm and a slice thickness of 1.5 mm (Fig. 4). All three acquisitions lasted 8.8 s and involved 16 segments, corresponding to a 16-fold acceleration relative to the fully sampled Cartesian reference with an acquisition duration of 2 min 20 s for 11 slices. The subsampling factor was in that case $R = 1.33$, as the long readout duration of 30.72 ms allowed the measurement of many samples

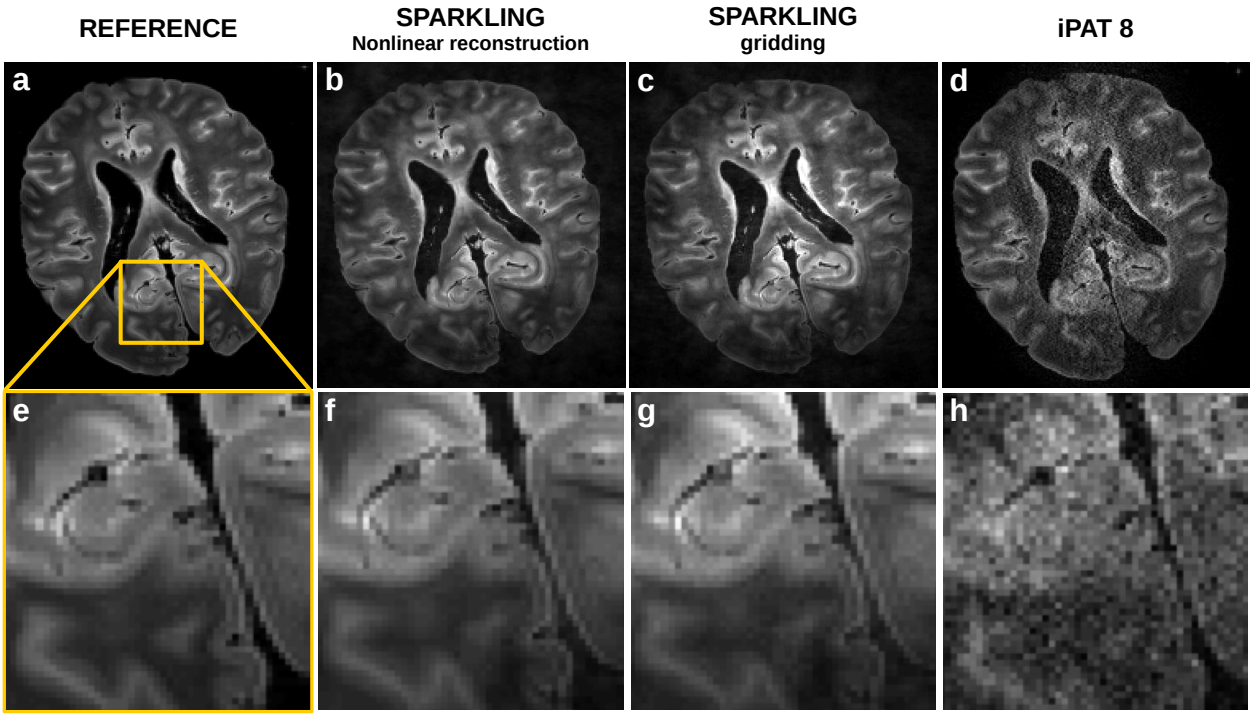

Figure 3: **Prospective validation of SPARKLING trajectories**. Acquisitions performed on a *ex vivo* human brain for uniform-density SPARKLING sampling (Fig. 1a output) at a resolution of 780 μm $\times$ 780 μm $\times$ 1.5 mm and an acceleration factor of $AF = 8$ without subsampling ($R = 0.66$). **a**, A fully sampled Cartesian reference lasting 2 min 20 s for 11 slices. **b**,**f**, Image reconstructed using nonlinear methods from SPARKLING acquisition lasting 16 s. **c**, Image reconstructed from the same SPARKLING acquisition using a gridding method. **d**, Image acquired with the input Cartesian trajectory of (Fig. 1a) and reconstructed with a GRAPPA method available on a Siemens scanner (integrated parallel acceleration technology with a factor of 8), whose acquisition time was 16 s. **e**,**f**,**g**,**h**, Magnified region of interest in the medial part of the parieto-occipital cortex (delimited by a yellow square in **a**) of images **a**,**b**,**c**, and **d**, respectively. Image reconstructions did not include any correction of system imperfections.

per shot (3072 samples per shot). Using the same nonlinear reconstruction pipeline, the resulting images (top row) and corresponding magnified images of a region of interest in the medial parieto-occipital cortex (bottom row) are shown in (Fig. 4b-f) for the SPARKLING trajectory, (Fig. 4c-g) for the variable-density spiral trajectory and (Fig. 4d-h) for the radial trajectory. While the SPARKLING reconstruction remains similar to the fully sampled Cartesian reference (Fig. 4a-e), the high acceleration factor severely impairs the results of the variable-density spiral and radial reconstructions. The accelerated radial trajectory generates a blurry image, illustrating the inefficiency of oversampling radial spokes. The more efficient variable-density spiral trajectory produces a higher-quality image; however the image contains notable off-resonance artifacts along the cortical surface of the brain (Fig. 4c) as well as in finer structures visible in the magnified image (Fig. 4g). Acquisitions were also performed with a higher in-plane resolution of 390 μm and three acceleration factors $AF = 10, 15, 20$. The SPARKLING trajectories were initialized

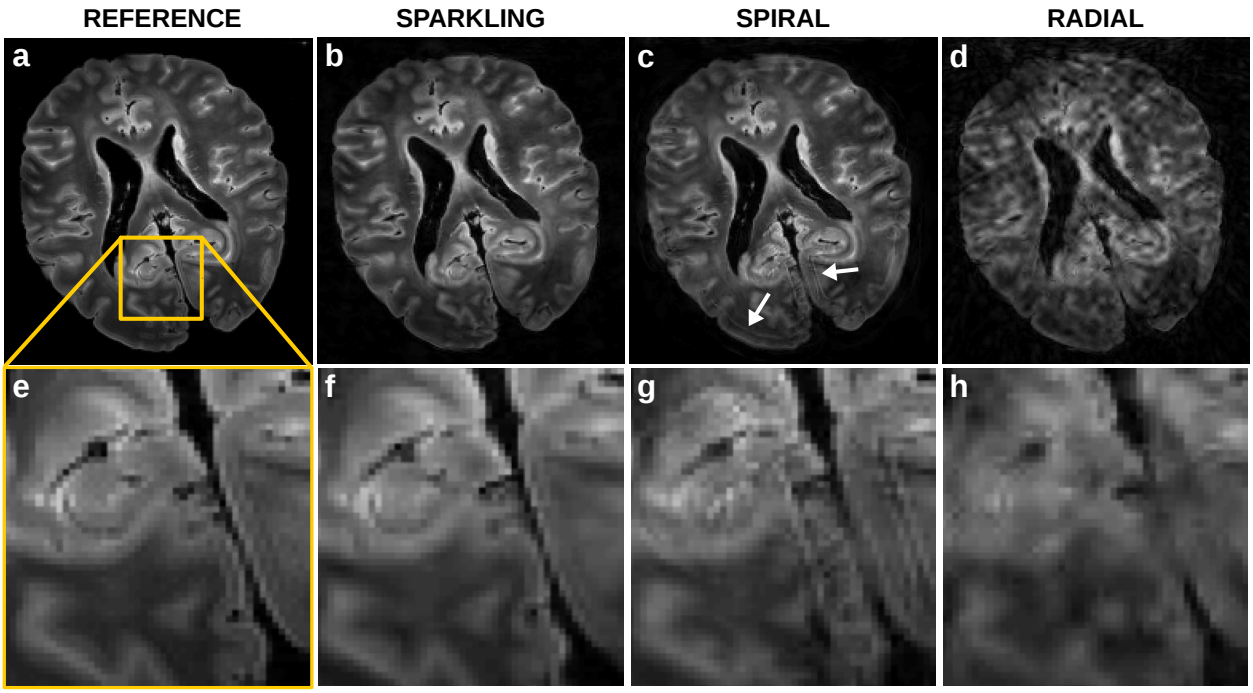

Figure 4: **Comparison of SPARKLING sampling with variable-density spiral and radial trajectories**. *Ex vivo* acquisition presenting a resolution of 780 μm $\times$ 780 μm $\times$ 1.5 mm, an acceleration factor of $AF = 16$ and a subsampling factor of $R = 1.33$. **a**, T_2^*-weighted reference image and a magnified region of interest in the parieto-occipital cortex in **e** acquired with a fully sampled Cartesian acquisition lasting 2 min 20 s for 11 slices. **b**,**f**, Image reconstructed from a 16-fold-accelerated SPARKLING-generated acquisition lasting 8.8 s. **c**,**g**, Image reconstructed from a 16-fold-accelerated variable-density spiral acquisition lasting 8.8 s. **d**,**h**, Image reconstructed from a 16-fold accelerated radial acquisition lasting 8.8 s. Image reconstructions did not include any correction of system imperfections. Image reconstructions did not include any correction of system imperfections.

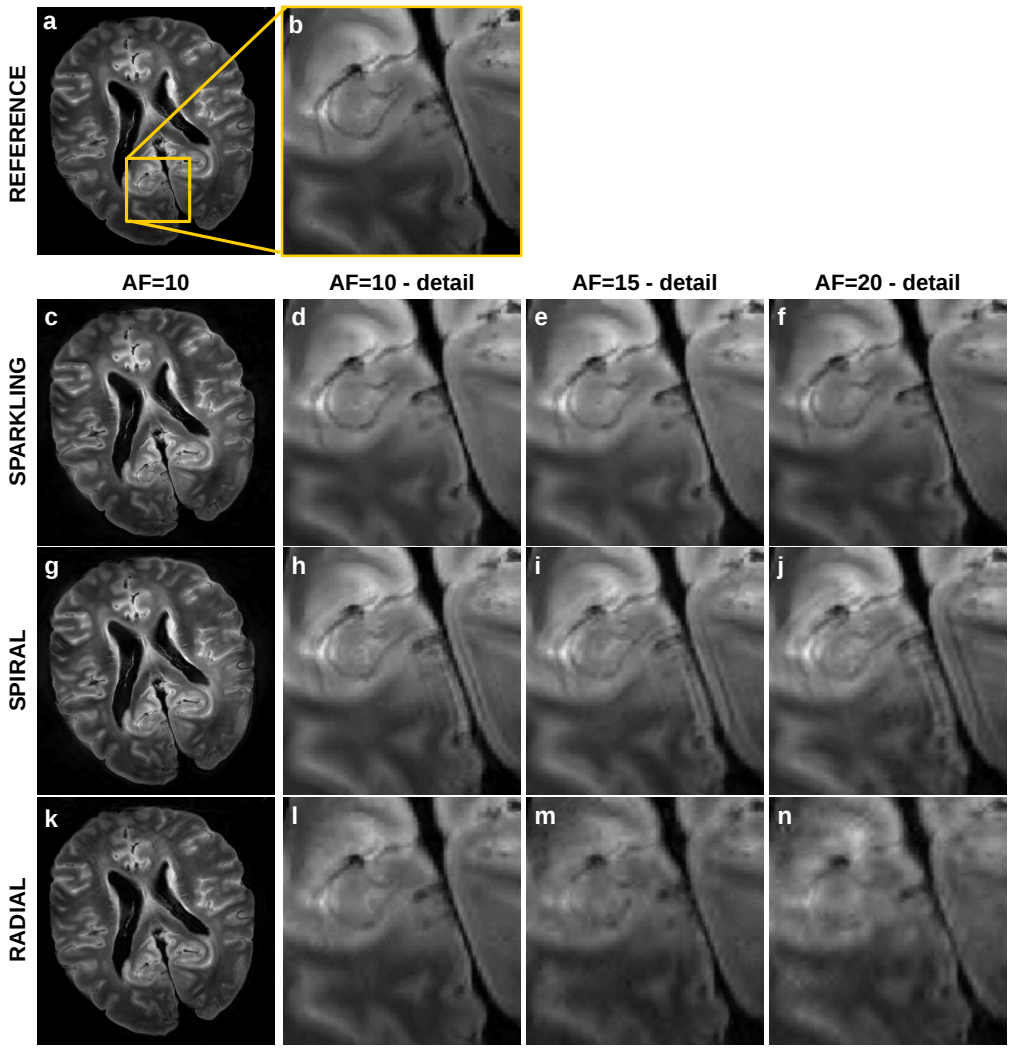

Figure 5: **Robustness of radial-initialized SPARKLING to very high acceleration factors**. Acquisitions performed on an *ex vivo* human brain for an image resolution of 390 μm $\times$ 390 μm $\times$ 3 mm and with acceleration factors ranging from $AF = 10$ to $AF = 20$. **a**,**b**, T_2^*-weighted reference image acquired with a fully sampled Cartesian acquisition lasting 4 min 42 s for 11 slices and a magnified region of interest in the parieto-occipital junction (delimited by the yellow box). Image reconstructed from 10-fold accelerated acquisitions (28 s) and magnified region of interest are respectively displayed in **c**,**d** for SPARKLING sampling, **g**,**h** for variable-density spiral sampling and **k**,**l** for radial sampling. Magnified images reconstructed from 15-fold accelerated acquisitions (18 s) are displayed in **e** for SPARKLING sampling, **i** for spiral sampling and **m** for radial sampling. Magnified images reconstructed from 20-fold accelerated acquisitions (14 s) are displayed in **f** for SPARKLING sampling, **j** for spiral sampling and **n** for radial sampling. Image reconstructions did not include any correction of system imperfections.

with radial patterns; the 15-fold accelerated SPARKLING trajectory corresponds to the output of

(Fig. 1b). The resulting SPARKLING images and corresponding magnified images are displayed in (Fig. 5c-d) for $AF = 10$, (Fig. 5e) for $AF = 15$ and (Fig. 5f) for $AF = 20$. When focusing on fine brain structures in the medial parieto-occipital cortex, the stability of image quality using SPARKLING trajectories with increasing acceleration factors is observed. In addition, the images produced with the SPARKLING sequence, despite their very short acquisition times, e.g. 14 s for the highest acceleration factor (Fig. 5f), maintain high similarity to the fully sampled Cartesian reference, which was obtained with an acquisition time of 4 min 42 s (Fig. 5a-b). Likewise, variable-density spiral and radial acquisitions with increasing acceleration factors are displayed in (Fig. 5g-h,i,j) and (Fig. 5k-l,m,n), respectively. In contrast to the SPARKLING reconstructions, the spiral acquisition yielded substantially more distortions due to off-resonance effects and the undersampled radial patterns produced an overly smoothed image presenting streaking artifacts at $AF = 20$.

In vivo experiments. T_2^*-weighted acquisitions were also performed *in vivo* on four healthy volunteers at an image resolution of 390 μm $\times$ 390 μm $\times$ 3 mm. Consistent with the *ex vivo* results, the *in vivo* results showed that the proposed SPARKLING strategy outperformed the conventional variable-density spiral and radial trajectories in all cases. The results from one subject are presented in (Fig. 6) for the highest studied acceleration factor, $AF = 20$. (Fig. 6b) shows the image reconstructed from the SPARKLING acquisition lasting 14 s, and this image is nearly indistinguishable from the reference (Fig. 6a), which was obtained in an acquisition time of 4 min 42 s for 11 slices. However, the spiral acquisition at the same acceleration factor (Fig. 6c,g) has notably more off-resonance artifacts, and the 20-fold-accelerated radial reconstruction (Fig. 6d,h) appears blurry and presents streaking artifacts.

Discussion

In this work, we demonstrated that gradient performance allows the successful use of more complex and efficient variable-density sampling patterns which are optimal for compressed sensing[42]. Using the non-Cartesian SPARKLING framework, it is hence possible to generate optimized sampling trajectories fulfilling the aforementioned key criteria of truly controlled sampling density, locally uniform coverage and controlled k-space path between consecutive samples. Given any MR protocol characterized by its echo time (TE) and readout duration (Tobs), the presented optimization-driven method is thus able to enhance MR sampling performance and reduce the number of shots in segmented acquisitions.

In this study, prospective accelerated acquisitions using SPARKLING trajectories were performed on a 7-Tesla scanner. The quality of these images was maintained at high in-plane resolutions of 390 μm and 780 μm both *ex vivo* and *in vivo*. The stability of this method was established even for very high acceleration factors of up to 20, at which fine structural details of T_2^*-weighted images were adequately preserved. The versatility of the SPARKLING approach in terms of initialization and density inputs was corroborated in practice with the implementation of both uniform and variable-density sampling initialized either with Cartesian lines or radial spokes.

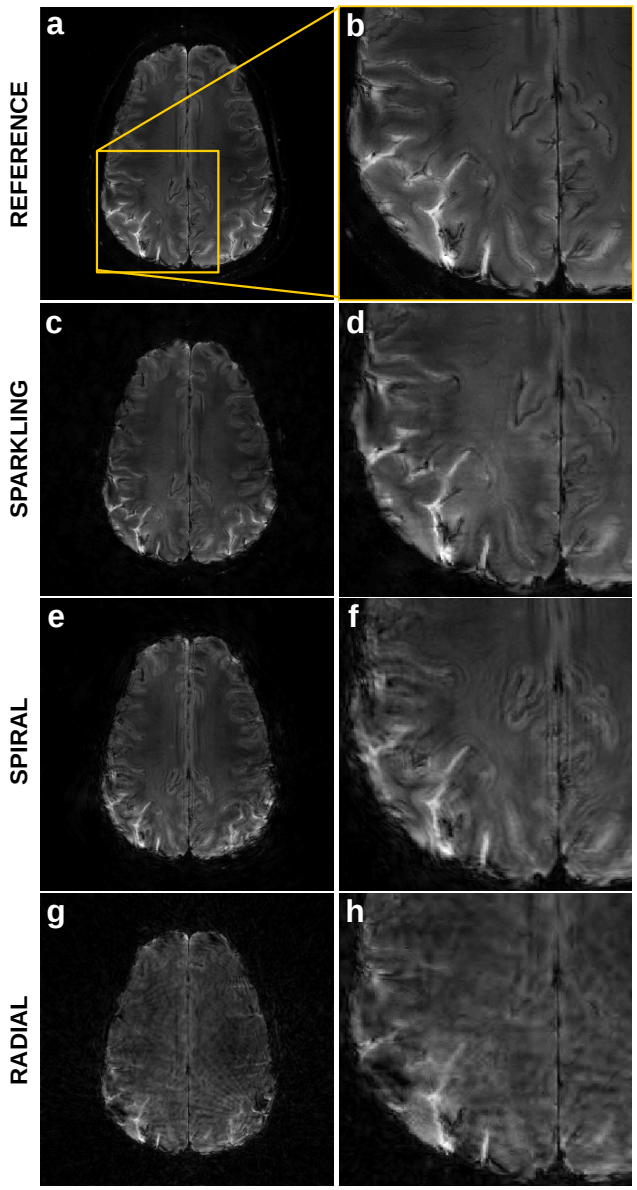

Figure 6: ***In vivo*** **validation of radial-initialized SPARKLING trajectories at an acceleration factor of 20 and comparison with spiral and radial sampling**. T_2^*-weighted GRE acquisition on a 7-Tesla scanner at an image resolution of 390 μm $\times$ 390 μm $\times$ 3 mm. **a**,**e**, Fully sampled Cartesian reference with an acquisition time of 4 min 42 s for 11 slices and a magnified region of interest in the parieto-occipital cortex (yellow box). **b**,**f**, Image and magnified image reconstructed from a 20-fold-accelerated variable-density SPARKLING acquisition lasting 14 s. **c**,**g**, Image and magnified image reconstructed from a 20-fold accelerated variable-density spiral acquisition lasting 14 s. **d**,**h**, Image and magnified image reconstructed from a 20-fold accelerated radial acquisition lasting 14 s. Image reconstructions did not include any correction of system imperfections.

Moreover, our sampling strategy was 5 to 7 times faster than the standard acceleration techniques available on the scanner (IPAT) to achieve acceptable image quality for T_2^*-weighting. Compared with conventional non-Cartesian spiral and radial 2D trajectories, the optimized variable-density SPARKLING sampling also yielded perceptually higher image quality. The similar results of *ex vivo* and *in vivo* imaging prove that motion was not a discriminating element in these cases. Despite the long readout duration for the T_2^*-weighted acquisition (30.72 ms), our method was relatively less sensitive to system imperfections such as magnetic field inhomogeneity or trajectory errors, while spiral acquisitions presented important artifacts, as often reported in the literature[30,43–45]. In spite of its sinuous appearance, SPARKLING patterns did not seem to suffer much from trajectory distortions which usually lead to severe image artifacts especially in non-Cartesian scanning. This relative robustness may be explained by considering a simple linear and time-invariant model of the gradient system. Under this assumption, the gradient system's behavior is fully described by its impulse response functions, which are called the gradient impulse response functions (GIRF)[46]. Given the general low-pass characteristics of gradient coils and amplifiers, the self-term GIRFs can be approximated by low-pass filters. (Fig. 7) shows the effects of low-pass filtering on one shot of the spiral (in blue) and the radial-initizalized SPARKLING (in orange) trajectories used for the 20-fold accelerated *in vivo* experiments in (Fig. 6). The simulated errors are represented as arrows departing from the nominal trajectories in a magnified region of the k-space center. The error vectors tend to point in the direction of the inward-pointing normal. Compared to the spiral errors, the SPARKLING ones are not only smaller in magnitude but also present random directions. This simple experiment provides an insight on why the SPARKLING patterns may be less sensitive to gradient errors than spiral patterns, even though a full validation would require a dynamic field camera such as[47]. Our method thus offers an interesting alternative to spiral imaging.

There may be two obstacles to the enhanced performance of the proposed strategy for 2D imaging. First, the modest SNR associated with 2D acquisitions may reduce the effectiveness of our method, as for any other subsampled trajectory. Although our experiments benefited from relatively good SNR conditions owing to a strong magnetic field and the use of a multiple receiver coil, SNR limitations appeared beyond the highest presented in-plane resolution of 390 μm. The second potential limitation is the hardware capacity, namely, the maximum gradient amplitude, the maximum slew rate and the gradient and readout bandwidths, which together control the flexibility and thus, the efficiency of the k-space trajectory. In particular, the gradient raster time plays a critical role and should be as short as possible. Assuming a readout bandwidth larger or equal to the gradient bandwidth, the following practical rule for best SPARKLING use should be observed: the ratio of the number of gradient steps per shot to the image size should be as high as possible. As regards high resolution, long-readout scenarios will maximize this ratio and thus optimize SPARKLING performance, while short-readout acquisitions allow for less departure from simple geometric trajectories. When considering lower resolutions however, our method remains applicable and promising. Moreover, in view of the considerable efforts that are currently being invested to push the hardware limits of gradient systems[48], it is reasonable to expect further improvement of SPARKLING performance. The SNR limitation should be considerably mitigated by the use of 3D

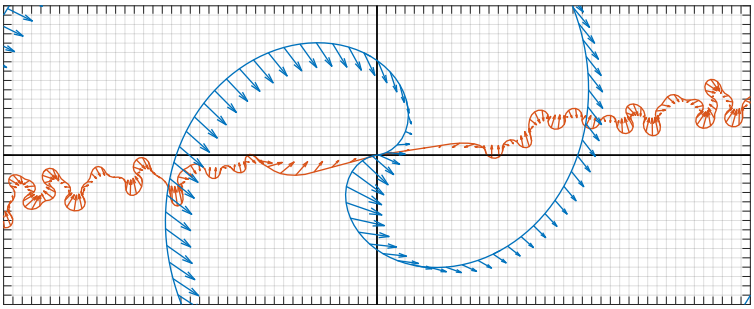

Figure 7: **Effects of low-pass filtering on spiral and radial-initialized SPARKLING shots**. To simulate trajectory errors, the gradients corresponding to an individual segment of a spiral trajectory (in blue) and a sparkling trajectory (in orange) were filtered with the same low-pass filter (for details, see Materials and Methods). A magnified region of the center of the k-space shows the nominal trajectories and the corresponding error vectors represented as arrows. Compared to the simulated trajectory errors of the spiral, the ones of SPARKLING are of smaller magnitude and present random directions. The gridded background corresponds to the Cartesian grid for the considered FOV.

SPARKLING acquisitions, which benefit from improved SNR conditions. Although our demonstration focused on 2D sampling as a proof of concept, the presented method can be extended to 3D imaging, for which further gains in terms of acceleration factors are anticipated. In this 3D setup, our framework would allow to generate sampling patterns with fully 3D variable density taking advantage of the undersampling potential in all three directions, in contrast to Poisson disk methods which sample along lines in the third direction[49]. Additional improvements may be achieved by incorporating corrections for field inhomogeneities and trajectory deviations into the reconstruction algorithms[50]; these possibilities have yet to be investigated. Most interestingly, in contrast to radial or spiral sampling methods, our technique is able to handle any arbitrary density (e.g., not necessarily radial) and therefore permits the implementation of anisotropic trajectories, which may lead to improved image reconstructions[51,52].

Our findings may be of value in numerous MRI applications including T_2^*[53,54], proton-density[55], susceptibility-weighted imaging (SWI)[56] and quantitative susceptibility mapping[57], as our method paves the way to increases in spatial and temporal resolution under conditions compatible with clinical time constraints. Our approach also allows to design optimized multi-echo acquisitions, which may be of interest for T_2^*-mapping[59,60]. By properly adjusting the initialization and target density of the proposed algorithm, any arbitrary sampling trajectory might be improved and potentially replaced. Given the advantage of SPARKLING sampling over radial sampling, substituting radial trajectories for patterns produced with our strategy would potentially enhance image quality or allow further acceleration. Furthermore, since each segment can be constrained to pass through the origin of the k-space at a given time, our SPARKLING trajectories possess valuable properties such as robustness to motion and potential for self-navigation (e.g., respiratory self-navigation), while remaining efficient. Most interestingly, our method can be readily used for

lower magnetic field imaging available in the clinic just by adapting the imaging protocol.

Methods

Design of SPARKLING trajectories. The design of SPARKLING trajectories was based on the theoretical work presented in[31,61], from which an iterative algorithm was derived to comply with criteria (i)-(iii). A k-space trajectory is usually composed of several segments $\boldsymbol{k}(t)$, also referred to as shots, which are controlled by magnetic field gradients $G(\tau)$ as follows :

$$\boldsymbol{k}(t) = \frac{\gamma}{2\pi} \int_0^t G(\tau) d\tau \tag{1}$$

Hardware constraints on the maximum gradient amplitude (G_{max}) and slew rate (S_{max}) induce limitations in trajectory speed and acceleration. These limits can be expressed as inequality range constraints on each of the time points of the discrete waveform $\boldsymbol{k}[i]_{1 \leq i \leq N}$:

$$\|\dot{\boldsymbol{k}}[i]\| = \left\| \frac{\boldsymbol{k}[i] - \boldsymbol{k}[i-1]}{\delta t} \right\| < \frac{\gamma}{2\pi} G_{max} \tag{2}$$

where δt is the gradient raster time. The constraint on the discrete trajectory acceleration is expressed likewise and criteria (iii) can easily be incorporated by adjusting the speed limitation to:

$$\|\dot{\boldsymbol{k}}[i]\| < \min\left(\frac{\gamma}{2\pi} G_{max}, \frac{1}{\text{FOV} \cdot \Delta t} \right) \tag{3}$$

where Δt is the sampling interval.

Following our previous work[15,31], our objective is to minimize the distance between a target density π and a sample distribution $\boldsymbol{k}$ under the aforementioned constraints :

$$\min_{\boldsymbol{k} \in \mathcal{Q}_p} dist(\pi, \nu(\boldsymbol{k})) = \min_{\boldsymbol{k} \in \mathcal{Q}_p} \frac{1}{2} \|h \star (\nu(\boldsymbol{k}) - \pi)\|_2^2 \tag{4}$$

where h is a continuous interpolation kernel, $\nu(\boldsymbol{k})$ is the measure supported by the curve $\boldsymbol{k}$ and $\mathcal{Q}_p$ is the set of admissible curves, i.e., respecting the aforementioned constraints.

The distance in (Equation 4) can be conveniently rewritten by expanding the L^2-norm into:

$$\min_{\boldsymbol{k} \in \mathcal{Q}_p} \underbrace{\frac{1}{N^2} \sum_{1 \leq i,j \leq N} H(\boldsymbol{k}[i] - \boldsymbol{k}[j])}_{F_r(\boldsymbol{k})} - \underbrace{\frac{1}{N} \sum_{i=1}^{N} \int_\Omega H(x - \boldsymbol{k}[i]) \pi(x)\, dx}_{F_a(\boldsymbol{k})} \tag{5}$$

where H is a well-chosen radial function (e.g. $H(x) = \|x\|_2$)[15,62]. (Problem 5) can be interpreted as the minimization of a potential energy containing an attractive term F_a (bringing together samples according to the target density) and a repulsive term F_r (avoiding the formation of gaps and clusters of samples). This non-convex cost function can be minimized by a gradient descent, after calculation of its derivatives. Altogether, a non-Cartesian algorithm was implemented on Matlab (Release 2015b, the MathWorks Inc., Natick, MA, USA) to solve (Problem 5) by means of a projected gradient descent which alternates between a non-convex distance minimization part and a projection onto the convex MR constraints. Compared to the previous works[31,61], we accelerated the convergence by using a Barzilei-Borwein step-size rule[63], allowing to double the algorithm speed. Importantly, all segments of an output SPARKLING trajectory are generated simultaneously using a multi-scale algorithm as shown in the supplementary videos. Typically, to generate the k-space trajectory in (Fig. 1a) (N=256, 32 shots, 3072 gradient points per shot, 5 decimation levels), the computation time was about 10 minutes on a Intel dual Core i7-5600U CPU running at 2.60 GHz with 16GB RAM.

The considered hardware constraints were $G_{max} = 40$ mT/m and $S_{max} = 200$ T/m/s for the gradient and the slew rate respectively. For T_2^*-weighted imaging, the readout time was set to 30.72 ms, corresponding to 3072 gradient samples. (Fig. 9a) displays the SPARKLING trajectory composed of 16 spokes of 3072 samples used to produce the brain image in Fig. (4b), corresponding to a 16-fold acceleration for an image size of 256×256.

Advanced discussion on the use of high sampling rate. The selection of the readout bandwidth is traditionally based on the Shannon-Nyquist criterion. Although matching Shannon's rate exactly does not convey stable reconstructions, it is well known that a small oversampling allows to design improved and stable linear reconstructions[64]. This explains why Cartesian trajectories for instance are usually sampled at twice the Shannon's rate. In the framework of linear reconstructions, using a higher bandwidth would arguably be unproductive because of the resulting higher computational burden. However, in the context of non-Cartesian sampling and nonlinear reconstructions, one faces the following dilemma: is it better to use a large sampling period, allowing to increase the per sample SNR or a shorter sampling period, yielding a larger number of noisier samples? In view of recent theoretical findings[33], we argue below that the latter solution should be preferred, especially in the case of our optimized trajectories. Although it is not clearly stated, the same idea seems to drive spiral acquisitions, where a high sampling rate is often used to rapidly sweep over a large portion of the k-space[30,32]. First, by increasing the bandwidth, the total number of samples is also larger, bringing additional valuable information for nonlinear reconstructions. More importantly, although the path traced out by k-space trajectories is continuous, the signal is sampled only at discrete intervals along the path. Because of the underlying bandlimiting filters of MR receiver hardware, the measured information is essentially averaged over short pieces of the continuous trajectories[34–36]. This explains why the per sample SNR increases as the bandwidth decreases, but it comes at the expense of a lower resolution in the k-space. The question is then: should SNR be preferred over k-space resolution? In view of the recent progresses in the field of nonlinear denoising[65], the answer seems to favor k-space resolution: it is usually much easier to denoise

data than solve complex deconvolution problems. There are however two practical reasons which may limit the bandwidth. First, a higher bandwidth produces more data which are harder to store and analyze. Fortunately, this aspect is mitigated by the use of massively parallel architectures such as GPUs. Second, since the ADC produces quantized data, it is critical to remain above the quantization step. In view of these arguments, we therefore set the sampling bandwidth equal to the gradient bandwidth, allowing to take full advantage of our erratic trajectories.

Target density. In this work, we address radially symmetric densities for the most part. The rationale for this choice is that we aimed to design sampling patterns that are *rotation and translation invariant*, i.e., that are capable of reconstructing images independently of arbitrary rigid transforms. This choice might be arguable since i) the organs (e.g., brain) are usually oriented in a unique position and ii) the sparsifying transform that we chose is not rotation invariant. However, the invariance requirement seems important for the design of *universal* sequences adapted to any organ.

In the situation in which all segments of a k-space trajectory pass through the origin at a given echo time, the sample density at the origin is excessively high. Our objective was to provide a method to generate target densities that mitigate this effect. Considering n_c segments crossing the origin with a maximum speed α, the minimal density in the center of the k-space is that of the radial trajectories at the maximum speed (see Fig. 8a). The density of the radial curves at a constant speed is of type $f(k) = \frac{c}{|k|}$ for a certain c (at least asymptotically as n_c increases). However, this is only true within a given disk D_{r_0} of radius r_0 that we wish to determine. In practice, the distance between two circularly adjacent samples (denoted $\Delta_{rad}(j)$ for the j_{th} sample from the center) should be smaller than $\tau\Delta k_0$, where $\tau \in (0, 1]$ and $\Delta k_0 = \frac{1}{FOV}$ is the size of a k-space pixel. Nyquist's theorem suggests taking $\tau = 1$, but selecting a lower value ensures more stability, as it allows the use of smooth interpolation functions[33]. The condition on two circularly adjacent samples $\Delta_{rad}(\bar{j}) \leq \tau\Delta_{k_0}$ therefore gives $r_{\min} = \bar{j}\alpha\Delta t$, where Δt is the sampling interval and the index $\bar{j}$ is given by:

$$\bar{j} = \left\lceil \frac{\tau\Delta_{k_0}}{\alpha\Delta t_{min}\sqrt{2 - 2\cos(\pi/n_c)}} \right\rceil. \tag{6}$$

Furthermore, to determine the density inside the disk D_{r_0}, we use the fact that the total mass of the density inside the disk should be $\frac{n_c(\bar{j}+1)}{m}$, where m is the total number of samples. The value of constant c defining the density f should be such that:

$$\int_{B_0^{r_{\min}}} f(k)\, dk = \frac{n_c(\bar{j}+1)}{m}, \tag{7}$$

i.e.,

$$c = \frac{n_c(\bar{j}+1)}{m\int_{B_0^{r_{\min}}} \frac{1}{|k|}\, dk}. \tag{8}$$

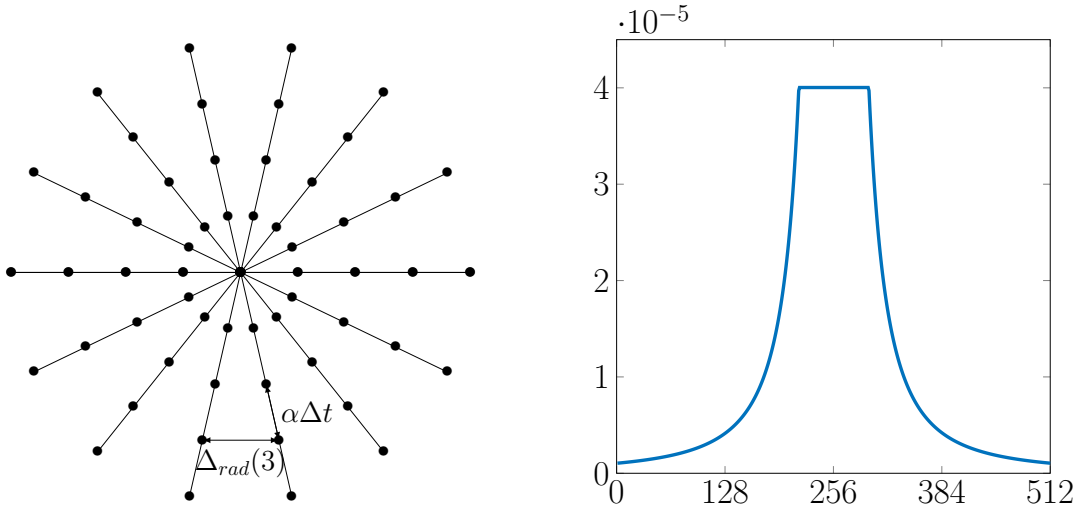

Figure 8: **Design of the target density**. (Left), The most rapidly vanishing density in the center of the k-space corresponds to the radial trajectories at the maximal speed. (Right), A representative density generated by our algorithm for N=512, $n_c = 34$, $d = 2$, $\tau = 0.5$, $\Delta t = 10$ μs, $\alpha = \gamma G_{max}$ and $G_{max} = 40$ mT/m.

Finally, we get:

$$f(k) = \frac{n_c(\bar{j}+1)}{m2\pi r_{\min}|k|}. \tag{9}$$

Given, an initial target density $\nu : k \mapsto \frac{1}{|k|^d}$, a value τ and the parameters describing the trajectory α, n_c and Δt, we generate an algorithm that returns a new target density π complying with the following three constraints:

1. Inside the disk D_{r_0}, $\pi = f$. Since the analytic expression of f was derived, it suffices to set $\pi(I) = f(I)$, where I is the set of indices with $|k| \leq r_{\min}$.

2. Two samples outside this disk should be separated by a distance greater than $\tau\Delta k_0$. The mean number of samples inside a pixel x of edge length Δ_{k_0} is $n_s\pi(x)$. If the samples are uniformly distributed in the pixel, the mean distance between adjacent pixels is $\frac{\Delta_{k_0}}{\sqrt{n_s\pi(x)}}$; we aimed for this distance to be greater than $\tau\Delta_{k_0}$. This means that π should satisfy:

$$\pi(x) \leq \frac{1}{n_s\tau^2} = \pi_{\max}. \tag{10}$$

3. π should be proportional to ν when possible. To satisfy this criterion, we designed an iterative algorithm as follows:

- While $\max(\pi(I^c)) > \pi_{\max}$
  - Find $J = \{k \in I^c, \pi(k) > \pi_{\max}\}$.
  - Set $\pi(J) = \pi_{\max}$.
  - Normalize π in $I^c \setminus J$.

For simplicity, we assumed that π is constant on each pixel of edge size Δk_0.

Design of spiral trajectories. Variable-density spiral trajectories were designed using a variable effective FOV as described in[66], with a maximum gradient amplitude of $G_{max} = 40$ mT/m, a maximum slew rate of $S_{max} = 200$ T/m/s. A symmetric segment was obtained by joining two opposing center-out spiral interleaves[67] in order for the echo time to be half of the readout time. The total duration of one interleaf was set to 30.72 ms by tuning the parameters controlling the linear variable-density trajectory. (Fig. 9b) displays the variable-density spiral sampling composed of 16 interleaves of 3072 samples used to produce the brain image in (Fig. 4c), corresponding to a 16-fold acceleration for an image size of 256×256.

Design of radial trajectories. Radial trajectories were designed using a trapezoid gradient waveform, with a ramp time of 0.1 ms until reaching a plateau amplitude of 0.98 mT/m and 1.96 mT/m for images sizes of $n = 256 \times 256$ and $n = 512 \times 512$, respectively, such that the readout time was 30.72 ms. Radial spokes crossed the origin of the k-space at their middle time point and were designed to reach the corners of the k-space. (Fig. 9c) displays the radial sampling composed of 16 spokes of 3072 samples each, which were used to produce the brain image in (Fig. 4d), corresponding to a 16-fold acceleration for an image size of 256×256.

Acquisitions. All acquisitions were performed on a 7-Tesla MR scanner (Siemens Healthineers, Erlangen, Germany) with a 1Tx/32Rx head coil (Nova Medical, Wilmington, MA, USA). The maximum gradient amplitude and slew rate for this system were 50 mT/m and 333 T/m/s, respectively. For the T_2^*-weighted acquisitions, a 2D GRE sequence was modified to allow execution of arbitrary gradient waveforms complying with the hardware constraints. All non-Cartesian trajectories were acquired using this sequence and the same parameters. The repetition time, echo time and observation time were 550 ms, 30 ms and 30.72 ms, respectively. The FOV was 20 cm, and the flip angle was 25 degrees. Two resolutions were investigated: 390 μm $\times$ 390 μm $\times$ 3 mm and 780 μm $\times$ 780 μm $\times$ 1.5 mm, corresponding to matrix sizes of 512×512 and 256×256, respectively. Standard shimming was performed on the studied slice for *ex vivo* acquisitions and on the whole brain volume for *in vivo* experiments. The sampling bandwidth was equal to the gradient bandwidth: rBW $= \text{BW}_{\text{gradient}} = 100$ kHz.

For the 8-fold accelerated Cartesian acquisition using online GRAPPA reconstruction (Fig. 3d-h), the same GRE sequence was used with Integrated Parallel Acceleration Technology. This sequence acquires 24 reference lines for auto-calibration. Sequence parameters were the same as above and the default oversampling factor of 2 was used for a base resolution of 256.

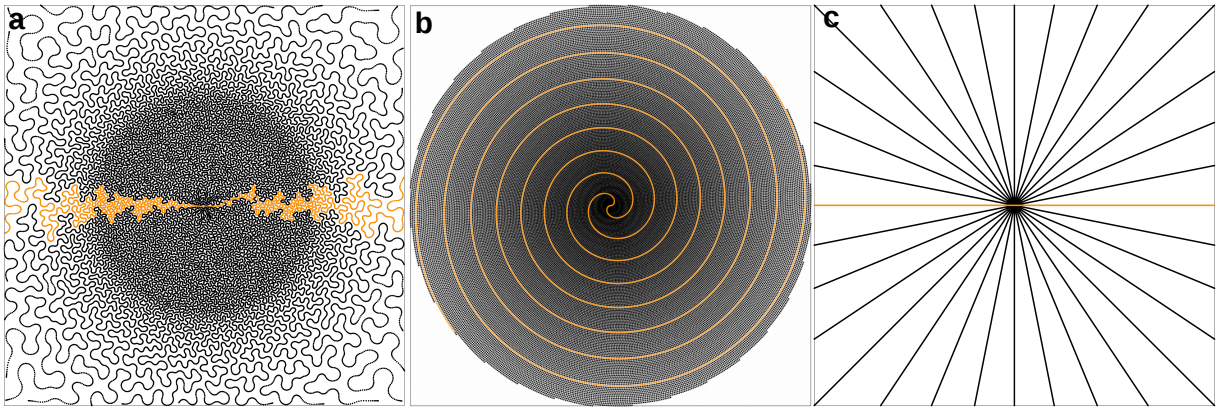

Figure 9: **Sampling trajectories used for (Fig. 4)**. The SPARKLING (**a**), variable-density spiral (**b**) and radial (**c**) trajectories used for *ex vivo* comparisons in (Fig. 4). The considered imaging matrix was 256×256, corresponding to a resolution of 780 $\mu m \times 780$ μm. Each trajectory is composed of 16 symmetric segments of 3072 samples (an individual shot is highlighted in yellow), resulting in an acceleration factor of $AF = 16$ and a subsampling factor of $R = 1.33$. An individual segment is highlighted in yellow.

***Ex vivo* experiments.** The human brain used for this study was obtained via the body donation program of University of Tours, France from a donor who gave his written consent before death. The brain was extracted and fixed in formalin (formaldehyde solution at 37 % m/m, Cooper, Melun, France) diluted in tap water to obtain a formalin concentration of 10 %). The *ex vivo* phantom was then immersed in a proton-free perfluorinated liquid before the acquisitions.

* *In vivo* experiments. The *in vivo* human experiments were approved by a national ethics committee (CPP IDF 7 Kremlin-Bicêtre) under the protocol registration number 07-042. All volunteers signed a written informed consent form.

Self-calibrating nonlinear reconstruction. 2D MR image reconstructions were performed by iteratively minimizing a sparsity promoting regularized Compressed Sensing SENsitivity Encoding (CS-SENSE) criterion introduced in[68–70]. We adopted a synthesis formulation composed of one ℓ_2-norm data consistency term and one ℓ_1-norm penalty term, which reads as follows:

$$\widehat{\mathbf{z}} = \underset{\mathbf{z}\in\mathbb{C}^{N\times N}}{\arg\min} \frac{1}{2} \sum_{\ell=1}^{L} \|F_\Omega \mathbf{S}_\ell \mathbf{\Psi} \mathbf{z} - \mathbf{y}_\ell\|_2^2 + \lambda \|\mathbf{z}\|_1. \tag{11}$$

This function estimates the image decomposition ($\widehat{\mathbf{z}}$) in a sparsifying domain before projecting the values back to the image domain, i.e., $\widehat{\mathbf{x}} = \mathbf{\Psi}\widehat{\mathbf{z}}$ with $\widehat{\mathbf{x}} \in \mathbb{C}^{N\times N}$, where $\mathbf{\Psi}$ was chosen as an orthogonal wavelet transform using the Symmlet of order 8 as the mother wavelet basis function $\Psi(t)$. We used $J = 4$ levels of decompositions, i.e., 12 sub-bands of detail coefficients for encoding horizontal, vertical and diagonal details on top of the low-frequency approximation. The sum of

squares term in (11) encodes parallel reception over the $L = 32$ channels of our phased array coil. $\mathbf{y}_l \in \mathbb{C}^m$ represents the measured Fourier values of the ℓ^{th} coil. To handle non-Cartesian Fourier samples, the non-equispaced fast Fourier transform (NFFT, version 3.2.3)[71] was therefore used to compute F_Ω. The NFFT takes non-uniformly sampled k-space measurements as input data and returns an image on the Cartesian grid. Matrix $\mathbf{S}_\ell \in \mathbb{C}^{n\times n}$ ($n = N \times N$) in (11) is diagonal and represents the sensitivity map associated with the ℓ^{th} coil that enhances the specific spatial domain of the desired image $\widehat{\mathbf{x}}$. To estimate the sensitivity maps $\{\mathbf{S}_\ell\}_{\ell=1:L}$, we extended a self-calibrated method used in SAKE[72] or IRGN[73] to the non-Cartesian setting, as explained below. First, for each coil, a low-resolution $N \times N$ image was reconstructed using the central surface representing 20 % of the collected k-space completed by zero-filling: $\mathbf{x}_\ell^{\text{LR}} = F^\star_{[\Omega_{|20\%},\mathbf{0}]}\mathbf{y}_\ell$, where LR stands for low resolution and F^* defines the adjoint operator of the NFFT. Second, the square root of the sum of squares (SSOS) was computed: $\mathbf{w} = \sqrt{\sum_{\ell=1}^{L} \|\mathbf{x}_\ell^{\text{LR}}\|^2}$. Third, the sensitivity maps were given by the pixelwise ratio of the low-resolution image coils and the SSOS: $[\boldsymbol{s}_\ell]_i = \text{diag}[\mathbf{S}_\ell]_{ii} = \left[\mathbf{x}_\ell^{\text{LR}}\right]_i / \mathbf{w}_i$, $\forall \ell = 1 : L, (i = 1 : n)$. Because of this SSOS operation, our method is less dependent on the threshold (i.e., 20 %) over the central surface of the k-space than the method of[74], who directly exploits the $\mathbf{x}_\ell^{\text{LR}}$ images as sensitivity map information. Once the sensitivity maps were estimated, an accelerated proximal gradient method[75] was implemented to solve (11). The regularization parameter λ controls the trade-off between data consistency and confidence in the sparsity prior, and this parameter was tuned manually over a discrete grid of values within the interval $[10^{-7}; 10^{-4}]$. In practice, we conducted image reconstructions for each value over this grid and retained the setting with the highest visual quality.

Low-pass filtering experiment to simulate gradient errors. To produce (Fig. 7), low-pass filtering was performed on a spiral and a SPARKLING shots. The shots were selected from the 20-fold accelerated trajectories used for the *in vivo* prospective experiments. After bilateral zero-padding of corresponding gradient waveforms in the time domain, a low-pass constant kernel of width 20 was applied to the input gradients by multiplication in the Fourier domain as described in[8]. After inverse discrete Fourier transform, the output trajectories were obtained by time integration.

Legends of Supporting Information. SI Video 1: Video showing the iterations of the SPARKLING algorithm for a uniform target density and an initialization with 32 Cartesian lines as in (Fig. 1a). The multi-scale algorithm was run for 9 decimation levels, during which the number of samples is successively multiplied by two until the final number of samples is reached (3072 samples per shot). Each level comprised 150 iterations. The color of consecutive shots alternates between yellow and blue. **SI Video 2**: Video showing the iterations of the SPARKLING algorithm for a radially decaying target density and an initialization with 34 symmetric radial segments as in (Fig. 1b). The multi-scale algorithm was run for 6 decimation levels, during which the number of samples is successively multiplied by two until the final number of samples is reached (3072 samples per shot). Each level comprised 150 iterations. The color of consecutive shots alternates between yellow and blue.

Acknowledgements

We would like to express our gratitude to the donors involved in the body donation program of the *Association des dons du corps du Centre Ouest*, Tours, who made this study possible by generously donating their bodies for science. We would like to thank Cyril Poupon for making it possible to use the *ex vivo* phantom. We also wish to thank Franoise Geffroy and Erwan Selingue for their help in manipulating the *ex vivo* phantom. We would like to thank Nicolas Boulant and Vincent Gras for their insightful remarks. This research program was supported by a 2016 DRF Impulsion grant (COSMIC, P.I.: P.C.). C.L. was also supported by the CEA international PhD program.

References

1. Barnes, J. *et al.* A meta-analysis of hippocampal atrophy rates in Alzheimer's disease. *Neurobiology of Aging* **30**, 1711–1723 (2009).

2. Pruessner, J. *et al.* Volumetry of hippocampus and amygdala with high-resolution MRI and three-dimensional analysis software: minimizing the discrepancies between laboratories. *Cerebral Cortex* **10**, 433–442 (2000).

3. van der Kolk, A. G., Hendrikse, J., Zwanenburg, J. J., Visser, F. & Luijten, P. R. Clinical applications of 7T MRI in the brain. *European Journal of Radiology* **82**, 708–718 (2013).

4. Duyn, J. H. The future of ultra-high field MRI and fMRI for study of the human brain. *Neuroimage* **62**, 1241–1248 (2012).

5. Maclaren, J. *et al.* Measurement and correction of microscopic head motion during magnetic resonance imaging of the brain. *PloS One* **7**, e48088 (2012).

6. Federau, C. & Gallichan, D. Motion-correction enabled ultra-high resolution in-vivo 7T-MRI of the brain. *PloS one* **11**, e0154974 (2016).

7. Stucht, D. *et al.* Highest resolution in vivo human brain MRI using prospective motion correction. *PloS One* **10**, e0133921 (2015).

8. Vannesjo, S. J. *et al.* Retrospective correction of physiological field fluctuations in high-field brain MRI using concurrent field monitoring. *Magnetic Resonance in Medicine* **73**, 1833–1843 (2015).

9. Pruessmann, K. P., Weiger, M., Scheidegger, M. B., Boesiger, P. *et al.* SENSE: sensitivity encoding for fast MRI. *Magnetic Resonance in Medicine* **42**, 952–962 (1999).

10. Griswold, M. A. *et al.* Generalized autocalibrating partially parallel acquisitions (GRAPPA). *Magnetic Resonance in Medicine* **47**, 1202–1210 (2002).

11. Candès, E. J., Romberg, J. & Tao, T. Robust uncertainty principles: Exact signal reconstruction from highly incomplete frequency information. *IEEE Transactions on Information Theory* **52**, 489–509 (2006).

12. Donoho, D. L. Compressed sensing. *IEEE Transactions on Information Theory* **52**, 1289–1306 (2006).

13. Lustig, M., Donoho, D. & Pauly, J. M. Sparse MRI: The application of compressed sensing for rapid MR imaging. *Magnetic Resonance in Medicine* **58**, 1182–1195 (2007).

14. Adcock, B., Hansen, A. C., Poon, C. & Roman, B. Breaking the coherence barrier: A new theory for compressed sensing. *Forum of Mathematics, Sigma* **5** (2017).

15. Boyer, C., Chauffert, N., Ciuciu, P., Kahn, J. & Weiss, P. On the generation of sampling schemes for Magnetic Resonance Imaging. *SIAM Journal on Imaging Sciences* **9**, 2039–2072 (2016).

16. Dippé, M. A. & Wold, E. H. Antialiasing through stochastic sampling. *ACM Siggraph Computer Graphics* **19**, 69–78 (1985).

17. De Goes, F., Breeden, K., Ostromoukhov, V. & Desbrun, M. Blue noise through optimal transport. *ACM Transactions on Graphics (TOG)* **31**, 171 (2012).

18. Edelstein, W. A., Hutchison, J. M., Johnson, G. & Redpath, T. Spin warp NMR imaging and applications to human whole-body imaging. *Physics in Medicine and Biology* **25**, 751 (1980).

19. Mansfield, P. Multi-planar image formation using NMR spin echoes. *Journal of Physics C: Solid State Physics* **10**, L55 (1977).

20. Lauterbur, P. C. Image formation by induced local interactions: examples employing nuclear magnetic resonance (1973).

21. Bergin, C., Pauly, J. & Macovski, A. Lung parenchyma: projection reconstruction MR imaging. *Radiology* **179**, 777–781 (1991).

22. Glover, G. & Pauly, J. Projection reconstruction techniques for reduction of motion effects in MRI. *Magnetic Resonance in Medicine* **28**, 275–289 (1992).

23. Ahn, C., Kim, J. & Cho, Z. High-speed spiral-scan echo planar NMR imaging-I. *IEEE Transactions on Medical Imaging* **5**, 2–7 (1986).

24. Meyer, C. H., Hu, B. S., Nishimura, D. G. & Macovski, A. Fast spiral coronary artery imaging. *Magnetic Resonance in Medicine* **28**, 202–213 (1992).

25. Pipe, J. G. *et al.* Motion correction with PROPELLER MRI: application to head motion and free-breathing cardiac imaging. *Magnetic Resonance in Medicine* **42**, 963–969 (1999).

26. Jackson, J. I., Nishimura, D. G. & Macovski, A. Twisting radial lines with application to robust magnetic resonance imaging of irregular flow. *Magnetic Resonance in Medicine* **25**, 128–139 (1992).

27. Bilgin, A., Trouard, T., Gmitro, A. & Altbach, M. Randomly perturbed radial trajectories for compressed sensing MRI. In *Proceedings of the 16th annual meeting of ISMRM*, 3152 (Toronto, Canada, 2008).

28. Lustig, M., Lee, J. H., Donoho, D. L. & Pauly, J. M. Faster imaging with randomly perturbed, under-sampled spirals and ℓ_1 reconstruction. In *Proceedings of the 13th annual meeting of ISMRM*, 685 (Miami Beach, FL, USA, 2005).

29. Wang, H., Wang, X., Zhou, Y., Chang, Y. & Wang, Y. Smoothed random-like trajectory for compressed sensing MRI. In *Engineering in Medicine and Biology Society (EMBC), 2012 Annual International Conference of the IEEE*, 404–407 (IEEE, 2012).

30. Tan, H. & Meyer, C. H. Estimation of k-space trajectories in spiral MRI. *Magnetic Resonance in Medicine* **61**, 1396–1404 (2009).

31. Chauffert, N., Ciuciu, P., Kahn, J. & Weiss, P. A projection method on measures sets. *Constructive Approximation* **45**, 83–111 (2017).

32. Cline, H. E., Zong, X. & Gai, N. Design of a logarithmic k-space spiral trajectory. *Magnetic Resonance in Medicine* **46**, 1130–1135 (2001).

33. Daubechies, I. & DeVore, R. Approximating a bandlimited function using very coarsely quantized data: A family of stable sigma-delta modulators of arbitrary order. *Annals of mathematics* **158**, 679–710 (2003).

34. Bernstein, M. A., King, K. F. & Zhou, X. J. *Handbook of MRI pulse sequences.* (2004).

35. Cho, Z.-H. *Foundations of medical imaging* (Wiley-Interscience, 1993).

36. Ansorge, R. & Graves, M. J. *The Physics and Mathematics of MRI* (Morgan & Claypool Publishers, 2016).

37. Mainero, C. *et al.* In vivo imaging of cortical pathology in multiple sclerosis using ultra-high field MRI. *Neurology* **73**, 941–948 (2009).

38. Nayak, K. S. & Nishimura, D. G. Randomized trajectories for reduced aliasing artifact. In *Proceedings of the 6th Annual Meeting of ISMRM*, 670 (Sydney, Australia, 1998).

39. Tsai, C.-M. & Nishimura, D. G. Reduced aliasing artifacts using variable-density k-space sampling trajectories. *Magnetic Resonance in Medicine* **43**, 452–458 (2000).

40. Smith, T. B. & Nayak, K. S. MRI artifacts and correction strategies. *Imaging in Medicine* **2**, 445–457 (2010).

41. Jezzard, P., Clare, S. *et al.* Sources of distortion in functional MRI data. *Human Brain Mapping* **8**, 80–85 (1999).

42. Lustig, M., Donoho, D. L., Santos, J. M. & Pauly, J. M. Compressed sensing mri. *IEEE Signal Processing Magazine* **25**, 72–82 (2008).

43. Yudilevich, E. & Stark, H. Spiral sampling in magnetic resonance imaging-the effect of inhomogeneities. *IEEE Transactions on Medical Imaging* **6**, 337–345 (1987).

44. Mason, G. F. *et al.* A method to measure arbitrary k-space trajectories for rapid MR imaging. *Magnetic Resonance in Medicine* **38**, 492–496 (1997).

45. Börnert, P., Schomberg, H., Aldefeld, B. & Groen, J. Improvements in spiral MR imaging. *Magnetic Resonance Materials in Physics, Biology and Medicine* **9**, 29–41 (1999).

46. Vannesjo, S. J. *et al.* Gradient system characterization by impulse response measurements with a dynamic field camera. *Magnetic Resonance in Medicine* **69**, 583–593 (2013).

47. De Zanche, N., Barmet, C., Nordmeyer-Massner, J. A. & Pruessmann, K. P. NMR probes for measuring magnetic fields and field dynamics in mr systems. *Magnetic Resonance in Medicine* **60**, 176–186 (2008).

48. Weiger, M. *et al.* A high-performance gradient insert for rapid and short-T2 imaging at full duty cycle. *Magnetic Resonance in Medicine* **79**, 3256–3266 (2018).

49. Vasanawala, S. S. *et al.* Improved pediatric MR imaging with compressed sensing. *Radiology* **256**, 607–616 (2010).

50. Sutton, B. P., Noll, D. C. & Fessler, J. A. Fast, iterative image reconstruction for MRI in the presence of field inhomogeneities. *IEEE transactions on Medical Imaging* **22**, 178–188 (2003).

51. Kutyniok, G. & Lim, W.-Q. Optimal compressive imaging of Fourier data. *arXiv preprint arXiv:1510.05029* (2015).

52. Baldassarre, L. *et al.* Learning-based compressive subsampling. *IEEE Journal of Selected Topics in Signal Processing* **10**, 809–822 (2016).

53. Frischer, J. M. *et al.* Susceptibility-weighted imaging at 7 T: improved diagnosis of cerebral cavernous malformations and associated developmental venous anomalies. *NeuroImage: Clinical* **1**, 116–120 (2012).

54. De Guio, F. *et al.* Loss of venous integrity in cerebral small vessel disease: a 7-T MRI study in cerebral autosomal-dominant arteriopathy with subcortical infarcts and leukoencephalopathy (CADASIL). *Stroke* **45**, 2124–2126 (2014).

55. Kasper, L. *et al.* Rapid anatomical brain imaging using spiral acquisition and an expanded signal model. *NeuroImage* (2017).

56. Haacke, E. M., Xu, Y., Cheng, Y.-C. N. & Reichenbach, J. R. Susceptibility weighted imaging (SWI). *Magnetic Resonance in Medicine* **52**, 612–618 (2004).

57. Langkammer, C. *et al.* Fast quantitative susceptibility mapping using 3D EPI and total generalized variation. *Neuroimage* **111**, 622–630 (2015).

58. Glover, G. H. & Law, C. S. Spiral-in/out BOLD fMRI for increased SNR and reduced susceptibility artifacts. *Magnetic Resonance in Medicine* **46**, 515–522 (2001).

59. Bittersohl, B. *et al.* Feasibility of T 2* mapping for the evaluation of hip joint cartilage at 1.5 T using a three-dimensional (3D), gradient-echo (GRE) sequence: A prospective study. *Magnetic Resonance in Medicine* **62**, 896–901 (2009).

60. Denk, C. & Rauscher, A. Susceptibility weighted imaging with multiple echoes. *Journal of Magnetic Resonance Imaging* **31**, 185–191 (2010).

61. Chauffert, N., Weiss, P., Kahn, J. & Ciuciu, P. A projection algorithm for gradient waveforms design in Magnetic Resonance Imaging. *IEEE Transactions on Medical Imaging* **35**, 2026–2039 (2016).

62. Schmaltz, C., Gwosdek, P., Bruhn, A. & Weickert, J. Electrostatic halftoning. In *Computer Graphics Forum*, vol. 29, 2313–2327 (Wiley Online Library, 2010).

63. Barzilai, J. & Borwein, J. M. Two-point step size gradient methods. *IMA journal of Numerical Analysis* **8**, 141–148 (1988).

64. Aldroubi, A. & Gröchenig, K. Nonuniform sampling and reconstruction in shift-invariant spaces. *SIAM review* **43**, 585–620 (2001).

65. Chatterjee, P. & Milanfar, P. Is denoising dead? *IEEE Transactions on Image Processing* **19**, 895–911 (2010).

66. Lee, J. H., Hargreaves, B. A., Hu, B. S. & Nishimura, D. G. Fast 3D imaging using variable-density spiral trajectories with applications to limb perfusion. *Magnetic Resonance in Medicine* **50**, 1276–1285 (2003).

67. Law, C. S. & Glover, G. H. Interleaved spiral-in/out with application to functional MRI (fMRI). *Magnetic Resonance in Medicine* **62**, 829–834 (2009).

68. Wu, B., Millane, R., Watts, R. & Bones, P. Applying compressed sensing in parallel MRI. In *Proceedings of the 16th Annual Meeting of ISMRM*, vol. 1480 (Toronto, Canada, 2008).

69. Liu, B., Zou, Y. M. & Ying, L. Sparsesense: application of compressed sensing in parallel MRI. In *Information Technology and Applications in Biomedicine, 2008. ITAB 2008. International Conference on*, 127–130 (IEEE, 2008).

70. Boyer, C., Ciuciu, P., Weiss, P. & Mériaux, S. HYR^{2}PICS: Hybrid regularized reconstruction for combined parallel imaging and compressive sensing in MRI. In *Biomedical Imaging (ISBI), 2012 9th IEEE International Symposium on*, 66–69 (IEEE, 2012).

71. Keiner, J., Kunis, S. & Potts, D. Using NFFT 3—a software library for various nonequispaced fast Fourier transforms. *ACM Transactions on Mathematical Software (TOMS)* **36**, 19 (2009).

72. Shin, P. J. *et al.* Calibrationless parallel imaging reconstruction based on structured low-rank matrix completion. *Magnetic Resonance in Medicine* **72**, 959–970 (2014).

73. Uecker, M., Hohage, T., Block, K. T. & Frahm, J. Image reconstruction by regularized nonlinear inversion-joint estimation of coil sensitivities and image content. *Magnetic Resonance in Medicine* **60**, 674–682 (2008).

74. Yeh, E. N. *et al.* Inherently self-calibrating non-Cartesian parallel imaging. *Magnetic Resonance in Medicine* **54**, 1–8 (2005).

75. Taylor, A. B., Hendrickx, J. M. & Glineur, F. Exact worst-case convergence rates of the proximal gradient method for composite convex minimization. *preprint arXiv:1705.04398* (2017).